

# LONG WAVELENGTH ASTROPHYSICS

by

Liam Dean Connor

A thesis submitted in conformity with the requirements  
for the degree of Doctor of Philosophy  
Graduate Department of Astronomy and Astrophysics  
University of Toronto

© Copyright 2016 by Liam Dean Connor

# **Abstract**

Long Wavelength Astrophysics

Liam Dean Connor

Doctor of Philosophy

Graduate Department of Astronomy and Astrophysics

University of Toronto

2016

—

# Contents

<b>1</b>	<b>Beamforming</b>	<b>1</b>
1.1	Chapter Overview . . . . .	1
1.2	Introduction . . . . .	1
1.3	Theory and Implementation . . . . .	2
1.3.1	Geometric phase . . . . .	3
1.4	Pathfinder beamformer . . . . .	6
1.4.1	Instrumental phases . . . . .	6
1.4.2	First coherent light . . . . .	10
1.5	FRB VLBI search . . . . .	14
1.5.1	Motivation . . . . .	14
1.5.2	Implementation . . . . .	15
1.5.3	ARO FRB search . . . . .	17
1.5.4	Results . . . . .	20
1.6	Conclusion . . . . .	25
	<b>Bibliography</b>	<b>27</b>

# List of Tables

# Chapter 1

## Beamforming

### 1.1 Chapter Overview

This chapter outlines the basic theory behind digital beamforming, and describes the commissioning of the first beamformer on CHIME Pathfinder. This includes the synthesis of several different software packages, the implementation of a scheduler, and an automated point-source calibration daemon that removes drifting instrumental gains in real-time. We will also detail early pulsar work and the beamformer’s first light. This includes the first ever coherent pulsar observations taken with CHIME. Finally, the creation of an ongoing VLBI FRB search between the DRAO and ARO will be outlined, starting with a real-time 24/7 search of the Pathfinder’s synthetic beam. We discuss early results, including the false-positive rate and distribution, as well as the implications of a non-detection on the FRB brightness distribution,  $N(S)$ .

### 1.2 Introduction

Beamforming is a signal processing technique that allows for spatial filtering, and has greatly benefited a diverse set of fields from radar and wireless communications to radio astronomy (van Veen & Buckley, 1988). Whether being used in phased-array RADAR

(Zrnic et al., 2007), ultrasonic imaging (Macovski, 1983), or wide-band radio astronomy (Tingay et al., 2013), beamforming allows for heightened sensitivity or output to select spatial modes. This usually involves a sensor (in our case an antenna) being used alongside a processor (in our case, a computing cluster) (van Veen & Buckley, 1988). Modern astronomy will benefit greatly from this technology. Beamforming is particularly essential to CHIME. The pulsar back-end will rely on brute-force beamforming in order to track ten sources at a time, 24-7. The FRB experiment will FFT-beamform to generate 1024 fan-beams, in order to search them in real time for radio transients. Finally, the cosmology experiment has always left itself the option of beamforming, whose computing cost scales as  $N \log N$ , as an alternative to the full- $N^2$  correlation.

### 1.3 Theory and Implementation

By coherently combining the voltages of a multi-element array, sensitivity can be allocated to small regions of the sky and the array’s effective forward gain can be increased. The signal from each antenna,  $x_n$ , is multiplied by a complex weight whose phases,  $\phi_n$ , are chosen a priori to maximally destructively interfere radio waves in all directions but the desired pointing. After applying such weights, the signals from all antennas are combined to give the formed-beam voltage stream,  $X_{\text{BF}}$ .

$$X_{\text{BF}} = \sum_{n=1}^N a_n e^{i\phi_n} x_n \quad (1.1)$$

Here  $a_n$  are real numbers that can be used as amplitude weightings for the antennas. If we define a more general complex weighting,  $w_n \equiv a_n e^{i\phi_n}$ , and switch to vector notation, Eq. 1.1 becomes,

$$X_{\text{BF}} = \mathbf{w} \mathbf{x}^T. \quad (1.2)$$

In general,  $X_{\text{BF}}$  and  $\mathbf{x}^T$  will be functions of time and frequency. This is also true for  $\mathbf{w}$ , unless one needs a static, non-tracking beam – which is the case for the CHIME Pathfinder’s transient search, described in Sect. 1.5. We can write this explicitly as follows,

$$\mathbf{w}_{t\nu} = (a_1(\nu)e^{i\phi_1(\nu)}, a_2(\nu)e^{i\phi_2(\nu)}, \dots, a_N(\nu)e^{i\phi_N(\nu)}) \quad (1.3)$$

$$\mathbf{x}_{t\nu} = (x_1(t, \nu), x_2(t, \nu), \dots, x_N(t, \nu)). \quad (1.4)$$

The voltage stream,  $X_{\text{BF}}$ , is then effectively squared and integrated to give a visibility stream. In the case of CHIME,  $X_{\text{BF}}$  corresponds to a single polarization so to get the full Stokes information one must compute the north-south polarization’s autocorrelation, the east-west autocorrelation, and their cross-correlation. The Stokes vector can be written as,

$$\mathbf{S} = \begin{pmatrix} I \\ Q \\ U \\ V \end{pmatrix} = \begin{pmatrix} X_{\text{ew}}X_{\text{ew}}^* + X_{\text{ns}}X_{\text{ns}}^* \\ X_{\text{ew}}X_{\text{ew}}^* - X_{\text{ns}}X_{\text{ns}}^* \\ \Re(X_{\text{ew}}X_{\text{ns}}^*) \\ \Im(X_{\text{ew}}X_{\text{ns}}^*) \end{pmatrix}. \quad (1.5)$$

### 1.3.1 Geometric phase

We now need to calculate  $\phi_n$  across the array. Ignoring instrumental phases for now, one can compute the geometric phases for an antenna by projecting its position vector,  $\mathbf{d}_n$ , onto the pointing vector,  $\hat{\mathbf{k}}$ . This gives,

$$\phi_n = \frac{2\pi}{\lambda} \mathbf{d}_n \cdot \hat{\mathbf{k}}, \quad (1.6)$$

where we have taken  $\mathbf{d}_n$  to be the baseline vector between feed  $n$  and an arbitrary



reference point and  $\phi$  is the corresponding phase difference. A sketch for this is shown

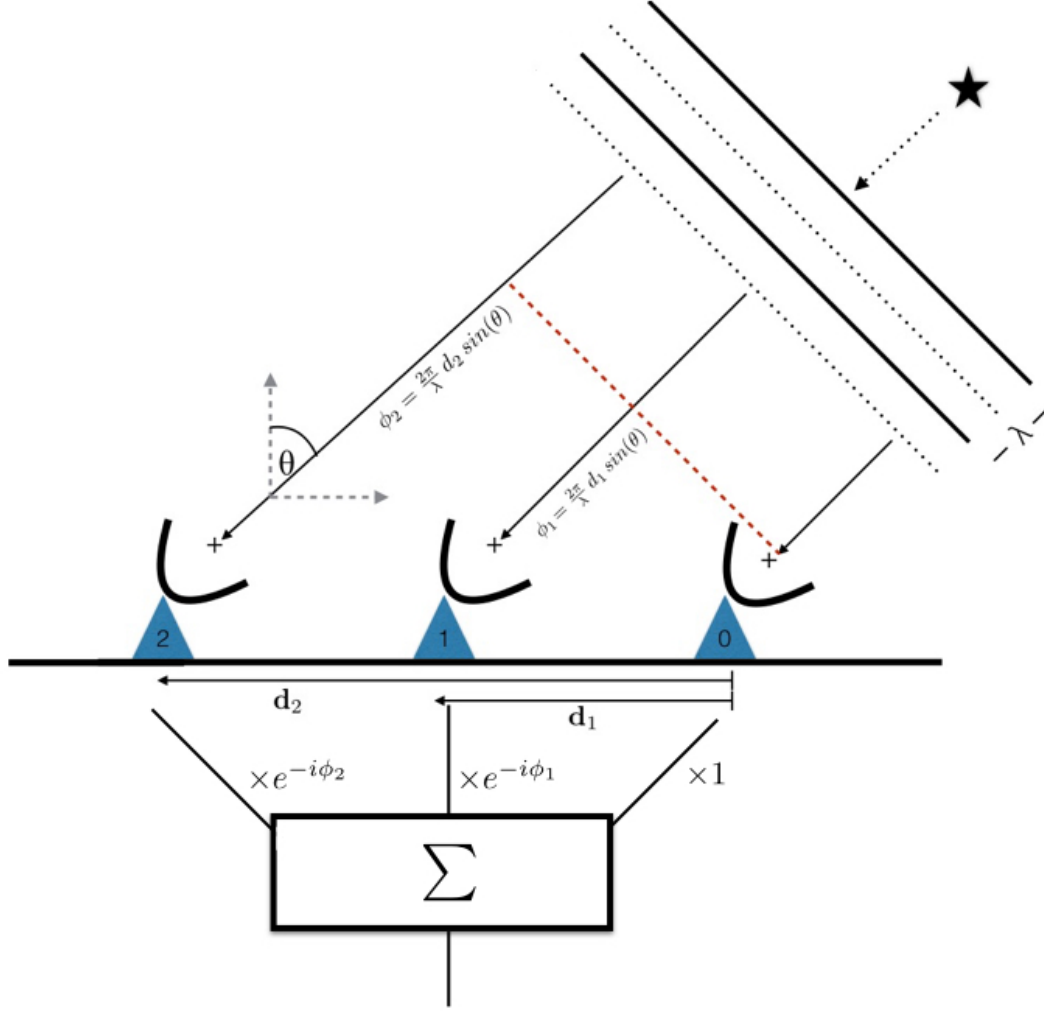


Figure 1.1: Diagrammatic example of a three-element beamformer. The wavefront from a far-field point-source arrives at each antenna at different times, but the delay is calculable given an array configuration and a direction to the object. Complex weights can be applied to each antenna's voltage time-stream to account for the geometric delay, allowing for the signals to be summed coherently.

To calculate the projection  $\mathbf{d}_n \cdot \hat{\mathbf{k}}$ , we need to go from celestial coordinates, in this case equatorial, to geographic coordinates. This requires only a source location, an observer location, and an observing time. For the latter we use local sidereal time (LST), which is the *RA* of the local meridian. This can be determined by an observer's longitude and a time, e.g. a Coordinated Universal Time (UTC). A source's hour angle is simply the

Variable	Coordinate
$\delta$	Source declination
$RA$	Source right ascension
$LST$	Local sidereal time
$HA$	Source hour angle
$alt$	Source altitude
$az$	Source azimuth
$lat$	Telescope latitude
$lon$	Telescope longitude

difference between  $LST$  and its  $RA$ ,

$$HA = LST - RA. \quad (1.7)$$

We use the standard interferometric  $(u, v, w)$  coordinate system to describe our baseline vector,  $\mathbf{d}_n$ . This is a right-handed coordinate system where  $u$  (east-west) and  $v$  (north-south) are in the plane whose normal is the zenith, and  $w$  measures the vertical direction (Thompson et al., 1986). They are defined in numbers of wavelengths, with  $u = d_{ew}/\lambda$ ,  $v = d_{ns}/\lambda$ , and  $w = d_{vert}/\lambda$ . Eq. 1.6 can be expanded as,

$$\phi_n = 2\pi (u, v, w) \cdot \hat{\mathbf{k}} \quad (1.8)$$

$$= 2\pi \left( u \hat{\mathbf{u}} \cdot \hat{\mathbf{k}} + v \hat{\mathbf{v}} \cdot \hat{\mathbf{k}} + w \hat{\mathbf{w}} \cdot \hat{\mathbf{k}} \right), \quad (1.9)$$

where each projection component can be obtained using spherical trigonometry. Though we do not go through the derivation here, it is given by the following product,

$$\mathbf{d}_n \cdot \hat{\mathbf{k}} = \lambda \begin{pmatrix} u, & v, & w \end{pmatrix} \cdot \begin{pmatrix} -\cos\delta \sin HA \\ \cos(lat) \sin\delta - \sin(lat) \cos\delta \cos HA \\ \sin(lat) \sin\delta + \cos(lat) \cos\delta \cos HA \end{pmatrix}. \quad (1.10)$$

These phases are not only essential to beamforming but also for the fringestopping process, which is ubiquitous in interferometric analysis and is described in Sect. 1.4.1.

## 1.4 Pathfinder beamformer

### 1.4.1 Instrumental phases

In a real experiment, if the voltages from each antenna,  $x_n$ , are summed without any adjustment from those written in Eq 1.1, one should only expect noise and not a coherent beam. This is because we have assumed the wavefront's differential time-of-arrival across the array is the same time delay seen by the correlator. In fact each signal is further delayed by multiple steps in the signal chain, often randomly. Digital phases in the electronics can be added by the LNAs and FLAs; coaxial cables, whose lengths vary by up to a meter, can rotate the signal by multiple radians. Therefore in order to coherently sum across the array and beamform, the instrumental phases must be removed. If  $e_n$  is the true electric field on the sky as seen by each feed, then the thing we measure is the on-sky signal altered by an effective gain,  $g_n$ , and a noise term,  $n_n$ .

$$x_n = g_n e_n + n_n \quad (1.11)$$

We have lumped several terms into  $g_n = |g_n|e^{i\phi_{g_n}}$ , which is composed of a pointing-dependent beam term and any complex gain introduced once light hits the cylinder. Since we care primarily about the phase, we can decompose  $\phi_{g_n}$  as,

$$\phi_{g_n} = \phi_{\text{beam}} + \phi_{\text{an}} + \phi_{\text{e}} + \phi_{\text{fpga}} \quad (1.12)$$

where  $\phi_{\text{beam}}$  is the beam's phase for a given pointing,  $\phi_{\text{an}}$  comes from the analog chain (dual-pol feed, coax, etc.),  $\phi_{\text{e}}$  is any phase introduced in the electronics, and  $\phi_{\text{fpga}}$  are phases applied in the F-engine.

Since the instrumental phases are effectively random, the simplest way to remove them is to solve for them empirically, usually from a point-source on the sky. The visibility definition from Eq. ?? in Chapter ?? can be written in terms of the electric field on the

sky instead of brightness temperature. The correlation between antennas  $m$  and  $n$  will be given by the following integral,

$$V_{m,n} = \int d^2\hat{\mathbf{k}} g_m(\hat{\mathbf{k}}) g_n^*(\hat{\mathbf{k}}) e_m(\hat{\mathbf{k}}) e_n^*(\hat{\mathbf{k}}), \quad (1.13)$$

where  $e_m(\hat{\mathbf{k}})$  is the complex electric field in the direction  $\hat{\mathbf{k}}$  as seen by antenna  $m$ . We can evaluate this all-sky integral as if the sky's electric field were produced by a single point-source. This is tantamount to a delta function at a single direction on the sky.

$$V_{m,n}^{\text{ps}} = \int d^2\hat{\mathbf{k}} g_m(\hat{\mathbf{k}}) g_n^*(\hat{\mathbf{k}}) e_m(\hat{\mathbf{k}}) e_n^*(\hat{\mathbf{k}}) \delta(\hat{\mathbf{k}} - \hat{\mathbf{k}}_{\text{ps}}) \quad (1.14)$$

$$= g_m(\hat{\mathbf{k}}_{\text{ps}}) g_n^*(\hat{\mathbf{k}}_{\text{ps}}) e_m(\hat{\mathbf{k}}_{\text{ps}}) e_n^*(\hat{\mathbf{k}}_{\text{ps}}) \quad (1.15)$$

In these equations  $\hat{\mathbf{k}}_{\text{ps}}$  is the only direction on the sky with a source in it — an approximation whose validity we will discuss below — and  $\delta$  is a Kronecker delta function.

If we explicitly write the phase information of the sky's electric field and write its magnitude as a brightness temperature, we get,

$$V_{m,n}^{\text{ps}} = g_m(\hat{\mathbf{k}}_{\text{ps}}) g_n^*(\hat{\mathbf{k}}_{\text{ps}}) T(\hat{\mathbf{k}}_{\text{ps}}) e^{2\pi i \hat{\mathbf{k}}_{\text{ps}} \cdot \mathbf{d}_{mn}}. \quad (1.16)$$

Therefore a single correlation can be written as an intensity multiplied by a phase factor that is determined by the source direction's projection onto that correlation's baseline. Since that phase factor is calculable via Eq. 1.10, it can be removed in a process called “fringestopping”. The data can be inspected visually quite easily, since a transiting point-source will fringe as a function of time at a rate corresponding to the projected baseline length, but should not after fringestopping is applied. This is demonstrated with an inter-cylinder Cygnus A transit in Fig. 1.2.

The visibilities we measure can be thought of as the upper triangle of an  $N \times N$

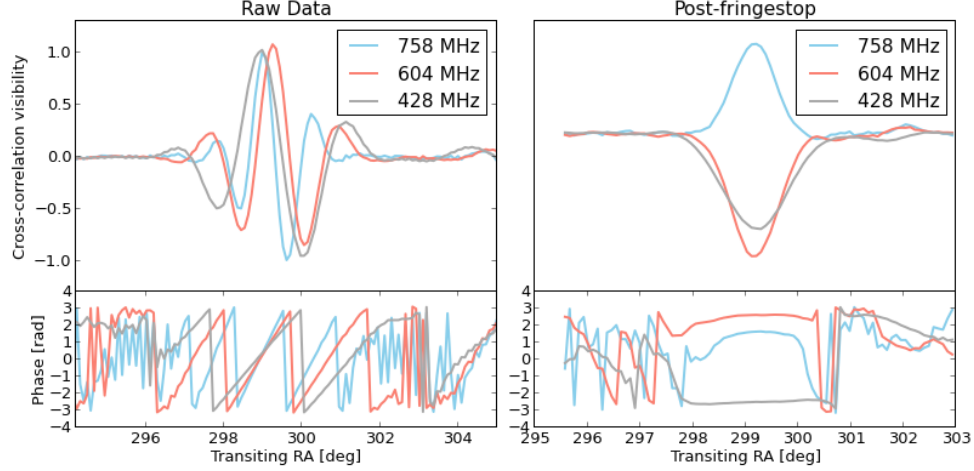


Figure 1.2: An example of the fringing process that is necessary for gain calibration off of a transiting point-source. Since the phase of a visibility will have a time- and frequency-dependent component, the measured correlation will fringe as the earth rotates in a chromatic way. This effect can be removed by multiplying each visibility by  $e^{-i\phi_{m,n}(t,\nu)}$ , as determined by Eq. 1.10. The top left panel shows the raw correlation between feeds 1 and 129 as a function of transiting  $RA$ , which are of the same polarization but on opposite cylinders, separated by 21 m. We plot three different frequencies. The panel below the top left shows the same complex visibility's phase. The slope, or fringe-rate, decreases at lower frequencies, as expected. The right panel show the same data after running it through the fringingstopping pipeline. Though the resulting phases are near flat, implying that the baseline is no long fringing, the visibilities are not purely real; this is because there are residual instrumental phases. These phases can be solved for using an eigendecomposition now that the array is phased up to a single point-source.

complex Hermitian matrix,  $\mathbf{V}$ . This is simply the outer product of the signal vector,  $\mathbf{x}$ , with its Hermitian conjugate.

$$\mathbf{V} = \mathbf{xx}^\dagger \approx \begin{pmatrix} |g_0|^2 e_0^2 & \dots & & \\ & & g_n g_m^* e_n e_m^* & \\ & & \ddots & \\ & & & |g_N|^2 e_N^2 \end{pmatrix} \quad (1.17)$$

If the sky is composed of a single point-source then this matrix will be rank one, i.e. there is only one non-zero eigenvalue. One can see this by referring to Eq. 1.16 and noting that if the data has been fringestopped, then the phase component (which is different for each correlation) goes away and the sky temperature (which is the same) can be factored out of Eq. 1.17, which becomes

$$\mathbf{V} = T(\hat{\mathbf{k}}_{\text{ps}}) \mathbf{g} \mathbf{g}^\dagger. \quad (1.18)$$

Therefore by diagonalizing the correlation matrix  $\mathbf{V}$  we get a complex eigenvector corresponding to the largest eigenvalue, and that eigenvector is proportional to the gain vector  $\mathbf{g}$ . The phase of this eigenvector will be an estimate for the instrumental phases,  $\phi_{g_n}$ , up to some unknown global offset. The goodness of this calibration depends on the validity of our assumption that the correlation matrix is rank one. We can estimate the error on the calibration solution as the ratio of the second largest eigenvalue,  $\lambda_2$ , to the largest,  $\lambda_1$ . For typical frequencies we get values of  $\frac{\lambda_2}{\lambda_1} \sim 2\%$  when using Cyg A or Cas A.

These algorithms have been implemented in a pre-beamforming pipeline written in **Python**. Every day a point-source transit is fringestopped and a calibration solution is solved for at each frequency. The source chosen depends on the solar time of its transit:

Since the sun is extraordinarily bright in our band it will be in our side-lobes as long as it is above the horizon, so the transit has to be at night for good calibration solutions. Historically, we have used Cygnus A in the spring and summer, Cassiopeia A in the summer and fall, and Tau A in the winter. Whatever we calibrate off of, the phases of that solution are written to pickle files that are then fed to the Pathfinder's FPGAs. The FPGA then applies complex gains after channelization, which in theory should provide the beamforming kernel with voltages whose phases are purely geometric.

### 1.4.2 First coherent light

Although the majority of the back-end was written within a couple of months, the beamformer required substantial on-sky testing and subsequent debugging. One important debugging tool came from utilizing the equivalence of the summed-and-squared high-cadence data that was produced by the beamformer with the full- $N^2$  integrated data. This is true because the correlation step does not erase any fundamental information about the electric field. The latter is nominally taken with  $\sim 21$  second time samples for 32,896 correlation products coming from 256 feeds. The former is a sum over the feeds which can be integrated in time arbitrarily after squaring. Ignoring the time rebinning for a moment, we can write the squared formed beam as,

$$X_{\text{BF}} X_{\text{BF}}^* = (w_1 x_1 + w_2 x_2 + \dots + w_N x_N)(w_1 x_1 + w_2 x_2 + \dots + w_N x_N)^* \quad (1.19)$$

$$= |w_1|^2 |x_1|^2 + \dots + |w_N|^2 |x_N|^2 + \dots + w_1 w_2^* x_1 x_2^* + w_2 w_1^* x_2 x_1^* + \dots, \quad (1.20)$$

where, as before,  $w_n$  are the complex weights applied in the beamformer and  $x_n$  is a voltage stream from antenna  $n$ . This can be rewritten as the sum of the auto correlations and twice the real part of the recorded phase-shifted cross-correlations.

$$X_{\text{BF}} X_{\text{BF}}^* = \sum_{n \leq N} |w_n|^2 V_{n,n} + 2 \sum_{\substack{n,m \leq N \\ n < m}} \Re\{W_{n,m} V_{n,m}\} \quad (1.21)$$

In this equation we have let  $W_{n,m} \equiv w_n w_m^*$ . Since the correlation matrix is Hermitian, its top and bottom triangles are redundant and one needs only to record  $\frac{1}{2}N(N+1)$  of the  $N^2$  pairwise products. If we wrote all pairwise correlations, we would simply need to sum the correlation matrix after applying the relevant weights, i.e. summing after the Hadamard product,  $\mathbf{W} \circ \mathbf{V}$ . This is identical to Eq. 1.21 if both matrices are Hermitian.

Using the equivalence we have just described, one can compare the output of the beamformer to the  $N^2$  visibilities after applying complex weights and summing the correlations. This is effectively off-line beamforming, though the cadence is too slow for the science goals of the real beamforming back-end, namely studying the time-variable sky. As a first test, we would form a stationary beam with only two feeds and let a bright point-source like Cas A drift through, producing a fringe pattern. We would then take the corresponding Cas A transit from the correlated “cosmology” acquisition, using Eq. 1.21 and giving only non-zero weights to the two relevant feeds, and check if the two fringe patterns were identical. We carried out a series of tests of escalating complexity, for example including more feeds in the sum, updating phases in real-time in order to track sources, and deliberately switching the weights with their conjugate to see if the fringe direction changed. Through these tests several bugs were discovered, including spherical trigonometry errors in the phase calculations and a disagreement between one piece of code’s definition of *LST*.

The final hurdle was more fundamental to CHIME’s architecture, though in principle it should not affect the cosmology experiment. It was found through early pulsar observations that the beamformer was only summing coherently when the instrumental phases that are removed in the FPGAs are solved for with the lower-triangle of the correlation



matrix. In other words, instrumental phases were not properly removed in the correlator unless they were applied as  $e^{+i\phi_{gn}}$  instead of  $e^{-i\phi_{gn}}$ , as one would expect. The perplexing thing was that in two years of analyzing the visibilities output by the correlator, nobody noticed a error in the sign-convention. And indeed, when we started to look at the phase of the raw visibilities, we found the argument of an east-west baseline increases with time, which is what one expects from an upper-triangle correlator. This apparent paradox was solved by discovering *two* sign reversals, one in the F-engine and one in the X-engine, that effectively cancel each other out, but only if both are applied.

Our digitizers sample at 800 MHz, taking advantage of the observing band between 400-800 MHz being in the second Nyquist zone. However, when we channelize the incoming time-stream data in the FPGAs, the complex conjugation associated with the aliased second Nyquist zone was not considered during the Fourier transform. Therefore the channelized voltages leave the F-engine with an opposite sign in the exponential. When they are correlated in the X-engine it is also done in reverse order as,

$$V_{n,m} = x_n^* x_m, \quad (1.22)$$

as opposed to the upper-triangle correlation described by Klages et al. (2015),

$$V_{n,m} = x_n x_m^*. \quad (1.23)$$

The second sign convention error does not affect the beamformed output, since that data stream is never correlated. We therefore needed to account for this for the back-end to work. An example of an early verification of the beamformer's sign convention and the first successful tracking observation is shown in Fig. 1.3. The collaboration has decided to keep these sign conventions as is and make note of it going forward, rather than re-write any low-level software.

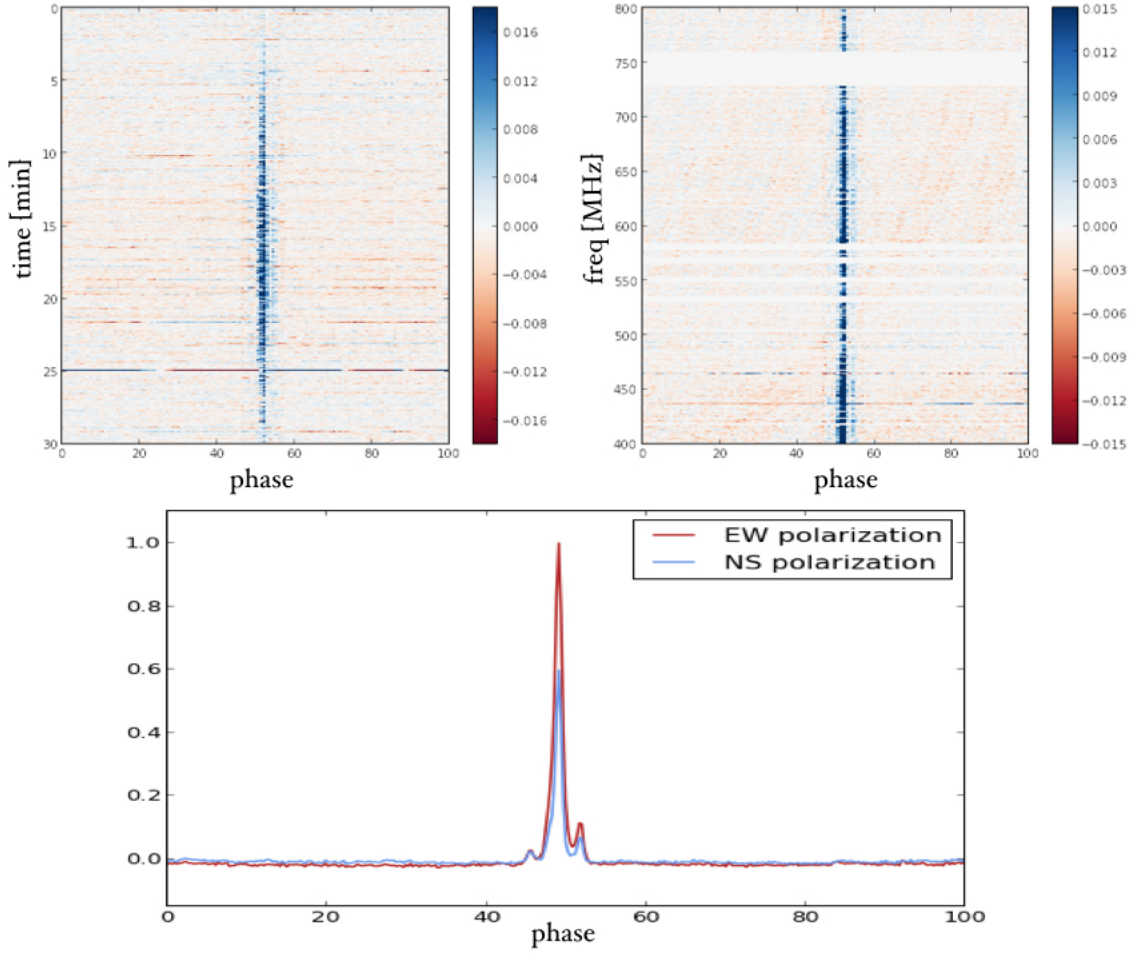


Figure 1.3: First coherent pulsar observations with CHIME. This brief observation of B0329+54 provided us with an idea of the instrument’s sensitivity and polarization response. Perhaps more significantly, it taught us that that our X-engine is a lower-triangle correlator, rather than upper-triangle like we thought, and that our F-engine *also* conjugates with the opposite sign. *top left*: waterfall plot of the pulsar’s Stokes I profile over the  $\sim 30$  minutes when the source enters then exits our beam. *top right*: frequency vs. phase Stokes I, integrated over roughly 15 minutes. *bottom*: time- and frequency-averaged pulse profile for the two polarizations autocorrelations. The difference between the east-west and north-south beams give an estimate for Stokes Q, which includes both intrinsic polarization ( $\sim 10\%$  for this source) and instrumental leakage.

## 1.5 FRB VLBI search

In 1967 Canada achieved an historic feat by doing the first ever successful very long baseline interferometry (VLBI) observation. The fringes were obtained between DRAO and ARO, with a baseline of 3,074 km (Broten et al., 1967). This result was given a “Milestone” award from The Institute of Electrical and Electronics Engineers (IEEE), which was also awarded for the inception of the Internet, transmission of transatlantic radio signals, and the discovery of Maxwell’s equations<sup>1</sup>. We have attempted to recreate the same VLBI baseline, but instead of using the considerable spatial resolution on quasars as in 1967, we are attempting to localize FRBs, and in place of the 26 m telescope we will use the Pathfinder’s formed beam.

### 1.5.1 Motivation

The CHIME Pathfinder is meant to have only one synthetic beam. Its purpose is primarily to act as a test-bed for the more powerful pulsar and FRB back-ends that will be attached to the full four-cylinder CHIME. However since the Pathfinder is on sky at all times and the beamformer we have built does not interrupt the ongoing cosmology acquisition, we decided to build a preliminary FRB search. We also have as many as three other telescopes onto which we can mount CHIME feeds and observe in our band: the Algonquin Radio Observatory (ARO), the John A. Galt 26m, and the Green Bank 140ft telescope. This would allow for the first ever VLBI detection of an FRB.

This is interesting for a few reasons. From a development standpoint it allows us to understand better various stages of the CHIME-FRB pipeline, including the rate of RFI false-positives, our algorithm’s search efficiency, and specs on the regularity and precision of instrumental gain removal. It will also give us a good sense of how the real CHIME beams behave on the sky.

Beyond just instrumental development, this work opens up several avenues for new

---

<sup>1</sup>[http://ethw.org/Milestones:List\\_of\\_IEEE\\_Milestones](http://ethw.org/Milestones:List_of_IEEE_Milestones)

science. Most interestingly, we could reasonably expect to see a few bursts per year in VLBI. Localization is by far the most important next step in determining the origin of FRBs, and such a long-baseline detection would achieve this. This particular VLBI array, whose baselines are thousands of kilometers, would provide the necessary spatial resolution to locate the source within its galaxy. This is demonstrated in Fig. 1.4. On top of this, we would not only detect a burst with milli-arcsecond resolution, but it would also be the first source in our band, at 400-800 MHz. We would be writing baseband and therefore full-polarization information, which is not true of most FRBs.

The Pathfinder beam could be used on its own to constrain the location of FRBs via their brightness distribution. Specifically, we could test the claims made by Vedantham et al. (2016) who suggest there is now evidence for a flat fluence distribution of FRBs, implying that they are cosmological in nature (see Chapter ?? for our detailed statistical analysis of this issue). This would mean there are a relatively large number of ultra-bright bursts, and that survey speed is determined by FoV rather than thermal sensitivity. The Pathfinder would be an excellent tool to test this hypothesis, as a non-detection after multiple months would call it into question.

Finally, during the search millisecond intensities could be written to disk. We can therefore look for slow pulsars and RRATS, since a significant fraction of the Galaxy transits each day.

### 1.5.2 Implementation

We have had a working beamforming back-end on the CHIME Pathfinder since October 2015. A beamforming kernel in the GPUs sends data over two 10 GBe lines to an acquisition node, `moose`, in the VLBI Data Interchange Format (VDIF) specification<sup>2</sup>. The back-end has been used primarily for short tracking pulsar observations, but had stability issues on timescales of  $\sim$ days, meaning we could not run it for long periods

---

<sup>2</sup>[http://www.vlbi.org/vdif/docs/VDIF\\_specification\\_Release.1.1.1.pdf](http://www.vlbi.org/vdif/docs/VDIF_specification_Release.1.1.1.pdf)

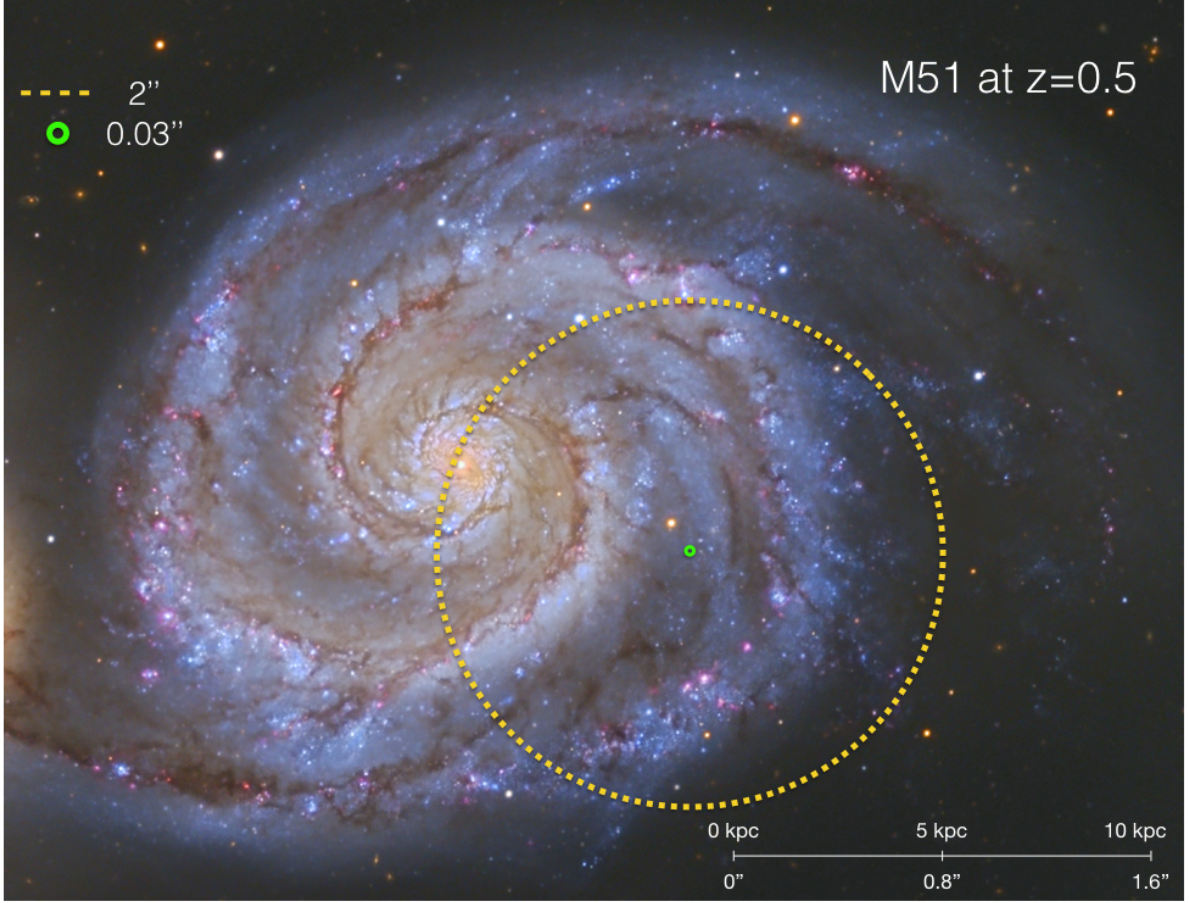


Figure 1.4: A visual demonstration of the difference between 30 milli-arcsecond resolution and an  $\sim$ arcsecond beam. This shows the need for extremely long baselines in a FRB VLBI effort. The image shows M51, which is about 20 kpc across, if it were at redshift 0.5.  $2''$  resolution ( $\sim 10^5$  wavelengths, or  $\sim 50$  km at 600 MHz.) cannot distinguish between the Galactic center and the edge of the disk. On the other hand,  $0.03''$  ( $\sim 10^7$  wavelengths) is the resolution of the 3,074 km DRAO-ARO baseline, which can localize the source well within the galaxy, even at high redshifts.

without interfering with the regular cosmology acquisition. However in the past several months a number of new features were added that allow not only long-term beamforming captures, but also transient searching.

A real-time, multithreaded acquisition code that takes in the VDIF packets coming out of the X-engine, and rearranges them to either be written to disk or search for FRBs<sup>3</sup>. Attached to this packet reader was a tree-dedispersion search code, some of

<sup>3</sup>[https://github.com/kmsmith137/ch\\_vdif\\_assembler](https://github.com/kmsmith137/ch_vdif_assembler)

which had been used before on Green Bank 100 m data and a real-time ARO search<sup>4</sup>. The CHIME acquisition software `kotekan` was altered in a number of ways, fixing the long-term stability issues in the beamforming kernel. These systems were synthesized into a real-time transient search back-end that has been on sky since May 2016. It is outlined in Fig. 1.5.2 on page 18.

Since CHIME is a transit telescope with a long north-south beam, our formed beam is effectively confined to the meridian. This means we must choose an optimal declination on which to park the beam. As a sanity check, we have spent roughly half the time pointed at the declination of pulsar B0329+54, which is the brightest switching source in the northern sky in our band. It is dispersed with  $26.833 \text{ pc cm}^{-3}$  and its individual pulses are bright enough to detect, meaning our tree-dedispersion algorithm ought to find its individual pulses. The search algorithm looks at time blocks of 100 seconds, searches for DMs between  $10\text{--}2000 \text{ pc cm}^{-3}$  with widths between 1-100 ms, and looks for peaks above  $8\sigma$ . If it finds something it “triggers” and writes out an image file containing the peak in DM / arrival time space, a dedispersed waterfall plot, a dedispersed pulse profile, and a fluence frequency spectrum. An example of the B0329+54 trigger output is shown in Fig.1.6. It also writes `numpy` arrays containing the squared and summed intensity data. It then moves on to the next block of 100 seconds, overlapping with the previous one by 18 seconds.

### 1.5.3 ARO FRB search

At ARO we have implemented a similar back-end to the one operating at DRAO. Luckily, the computing requirements are less demanding. Since there is only one dual-polarization feed mounted on the dish, we need only one FGPA board and one processing node. At DRAO  $1/16^{\text{th}}$  of frequencies are handled by each GPU node, which means they arrive scrambled at the acquisition machine, `moose` (see 1.5.2). Software had to be written to

---

<sup>4</sup>[https://github.com/kiyo-masui/burst\\_search](https://github.com/kiyo-masui/burst_search)

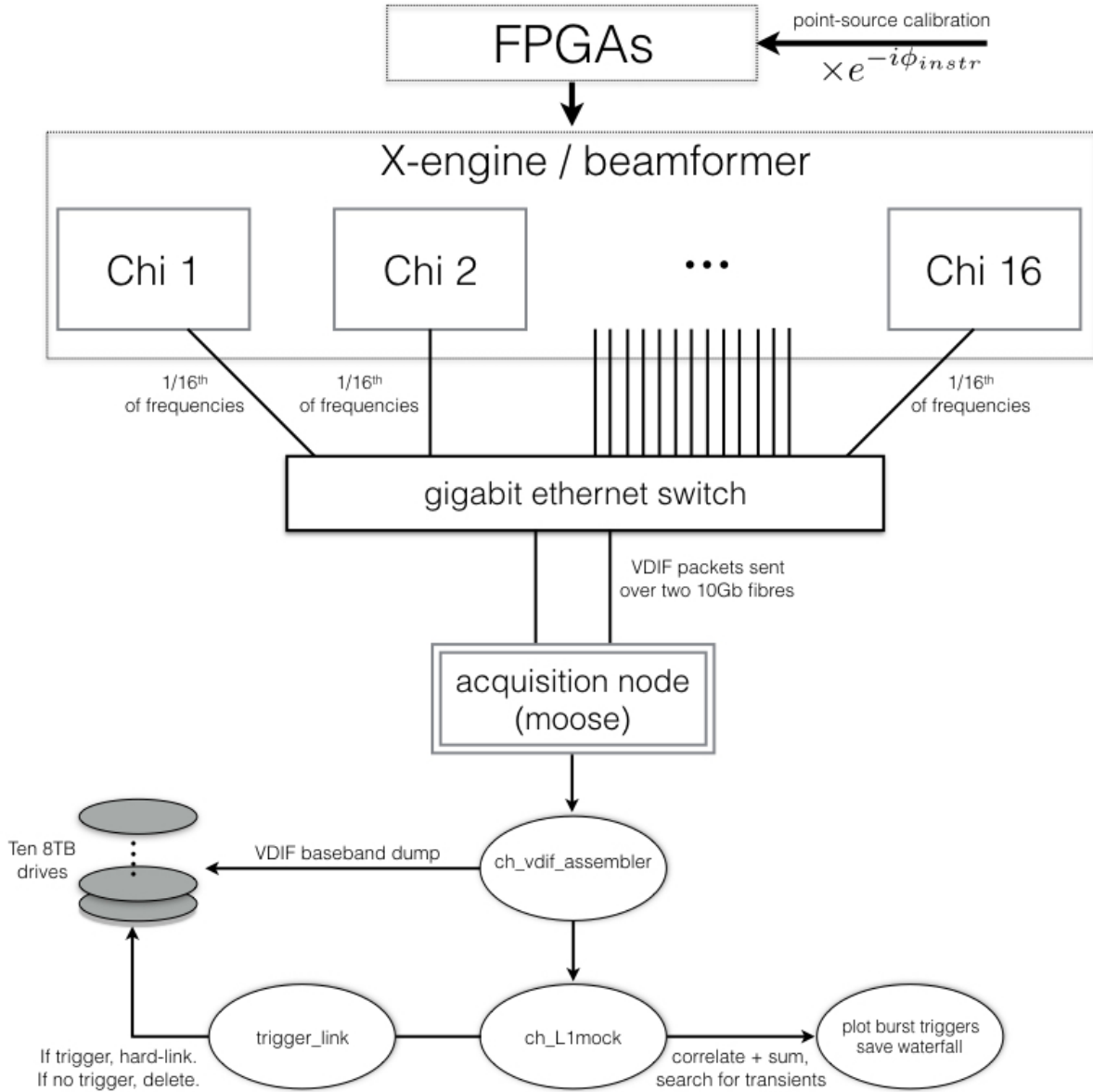


Figure 1.5: Block diagram of the beamforming back-end on CHIME Pathfinder. A calibration solution is obtained from a bright point-source transit, the phases of which are fed into the FPGAs where they are applied as a digital gain. All antenna signals are then sent the *X*-engine, comprised of 16 GPU nodes. Each node applies geometric phases then sums the voltage stream across all antennas with the same polarization. The two resultant beams are then sent to our acquisition machine *moose* as VDIF packets, where a multi-threaded capture code, *ch\_vdif\_assembler*. At this point the baseband data are either written to disk as scrambled baseband VDIF, or they are reorganized in time and frequency. The ordered data are searched for FRBs after squaring and integrating to  $\sim$ millisecond cadence using a tree-dedispersion algorithm. If there is a trigger, then the corresponding baseband data is hard-linked. Old files that haven't been hard-linked are deleted periodically.



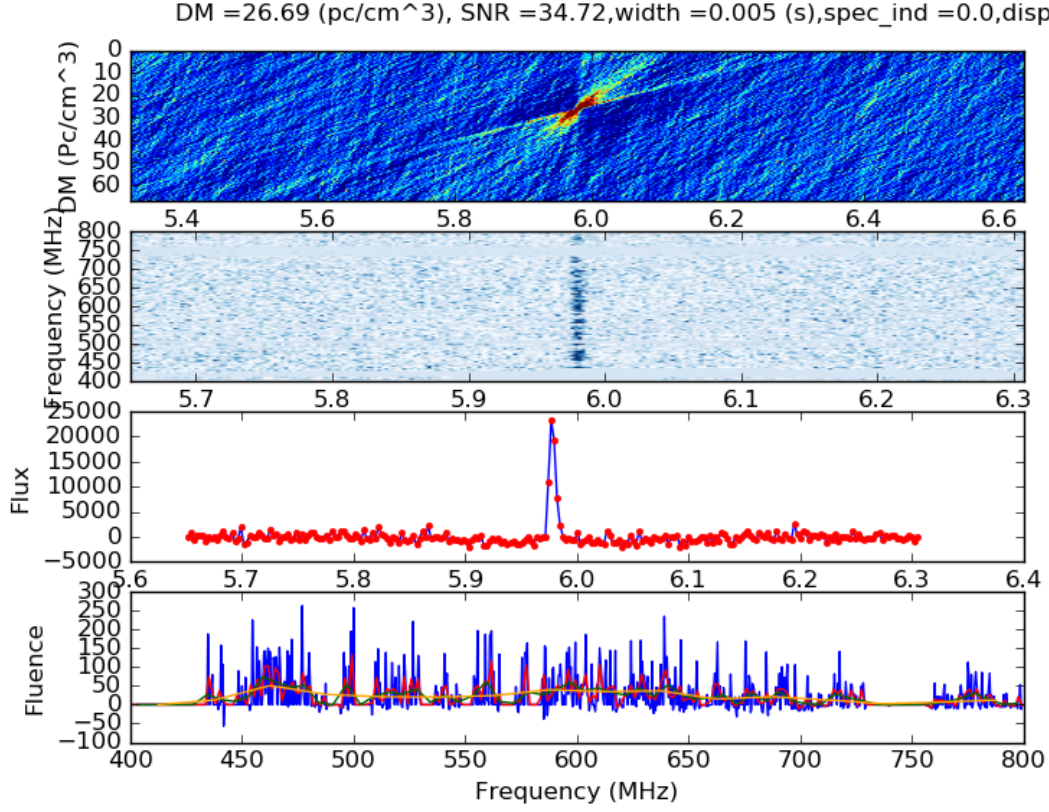


Figure 1.6: Example of a figure created after a trigger on the Pathfinder FRB search. This trigger was during the transit of pulsar B0329+54, on whose declination our synthetic beam was parked. Further information about the pulse is included at the top of the figure, including signal-to-noise ratio, width, and dispersion index. Though the beam is not well calibrated in absolute flux, this pulsar is of order 10 Jy, so this pulse might be half as bright as the original Lorimer burst (Lorimer et al., 2007). *Top panel:* The search results in dispersion measure vs. arrival time space. The red, butterfly-like cluster of points around DM of 25 pc cm<sup>-3</sup> and arrival time 6 seconds into the 100 second block, shows the detection of a single B0329+54 pulse. *Second panel:* A frequency vs. time colour map showing the dedispersed pulse. *Third panel:* Pulse profile for this trigger, averaged over frequency after masking RFI and weighting by inverse system temperature. *Bottom panel:* Fluence vs. frequency plot of the pulse.

re-order in time and frequency data in real-time. At ARO, all 1024 frequencies arrive in contiguous blocks at each frame, meaning we simply listen to a socket for the packets, square and sum, then search for FRBs. The ARO back-end is outlined in Fig. 1.7.



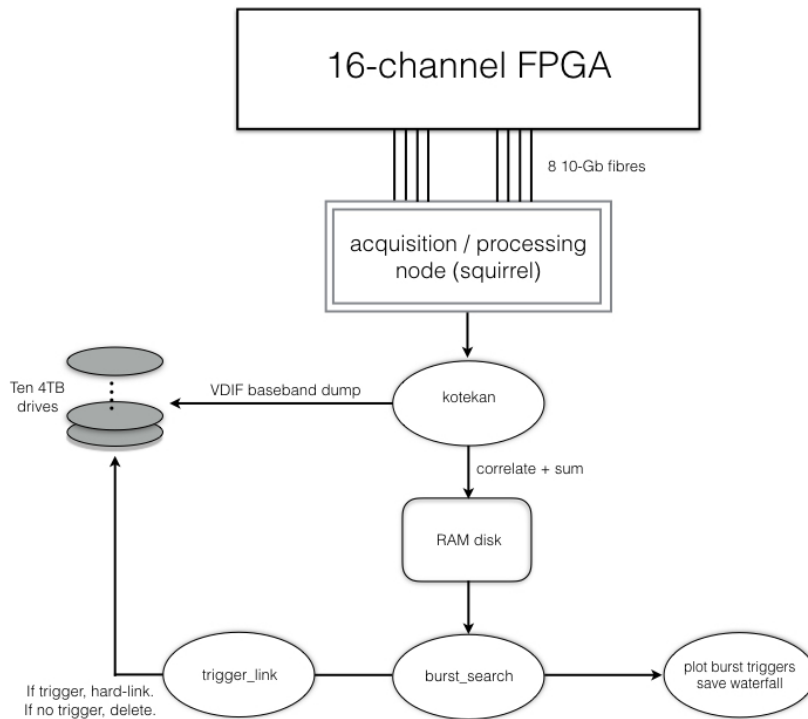


Figure 1.7: This figure shows a block diagram of the basic FRB search set-up at ARO. A single 16-channel FPGA channelizes the 800 Ms/s data and sends 1024 frequencies to an acquisition node, `squirrel`, at a cadence of  $2.56 \mu\text{s}$ . Those data are squared, summed, and dumped to a RAM disk, where it is searched for FRBs between  $10\text{-}2000 \text{ pc cm}^{-3}$ .

### 1.5.4 Results

#### A flat brightness distribution?

As we discuss in chapter ??, there is a large uncertainty in the FRB rate between 400-800 MHz. There is even greater uncertainty in the expected rate for a telescope like the CHIME Pathfinder. This is because at this time all FRBs have been detected with large collecting area, highly sensitive single-dish telescopes (GBT, Parkes, and Arecibo). Therefore in order to extrapolate the rate estimates on to the Pathfinder, which does not have much collecting area and whose beam is quite large, one needs to know the

underlying brightness distribution. As we will show in Chapter ??, the rate depends on the product of the telescope’s field-of-view (FoV) and a thermal sensitivity term. For a single-feed receiver, the FoV is given by  $\sim \left(\frac{\lambda}{D}\right)^2$ , which scales inversely with collecting area,  $A$ . The thermal component depends linearly on forward gain and therefore collecting area. Combining these, the rate is,

$$r_o = \text{FoV} \times (\text{sensitivity})^\alpha \quad (1.24)$$

$$\propto A^{-1} A^\alpha, \quad (1.25)$$

where  $\alpha$  is the FRB flux distribution’s power-law index, which is 3/2 if FRBs are non-cosmological and Euclidean. If  $\alpha < 1$ , as is expected in the cosmological FRB scenario, then small telescopes are actually advantageous over large single-pixel telescopes since the beamsizes becomes more important when  $\alpha - 1$  is negative.

With a dish like the Pathfinder we expect the detection rate to be roughly 10 times higher if  $\alpha \approx 0.8$  (cosmological scenario) compared to the Euclidean case. This is because its relatively low sensitivity per steradian requires there be large numbers of very bright bursts, which one gets from a flat distribution. Using non-detection in  $\sim 2$  months of observing, we can estimate the values of  $\alpha$  that are excluded by calculating the Poissonian probability of seeing zero given some expected value. As a simple model, assume the probability of seeing  $M$  events given some expected number of events  $\mu$ . Then,

$$P(M|\alpha, \mu) = \frac{\mu^M e^{-\mu}}{M!} \quad (1.26)$$

where  $\mu$  can be calculated by extrapolating from other surveys in which FRBs have been seen. If we take the Pathfinder daily rate estimated in (Connor et al., 2016) and presented in Chapter ?? and multiply it by the number of days on sky, we can calculate a  $p$ -value as a function of  $\alpha$ . This is just given by  $P(0|\alpha, \mu) = e^{-\mu}$  and it plotted in Fig. 1.8. We find that  $\alpha < 0.61$  can be ruled out with 95% confidence. This is based on the

Pathfinder sensitivity estimates we use in Chapter ??, with  $T_{\text{sys}} = 50$  K, only 100 MHz of bandwidth (for reasons we will discuss), and a S/N threshold of  $8.5\sigma$ . The dashed line on the right edge of the blue contour gives the probability of seeing zero FRBs in 45 days of observing, assuming the  $2\sigma$  upper-limit on the FRB rate in our band. The left edge uses the lower-bound on the rate, which is why seeing no events is quite likely, even when the spectrum is quite flat.

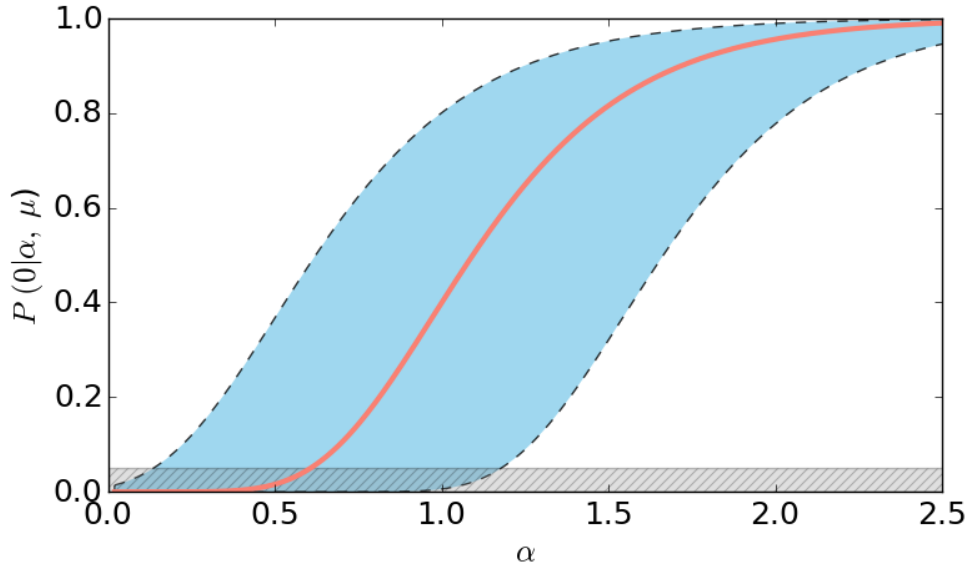


Figure 1.8: Early limits on the brightness distribution parameter  $\alpha$  from the Pathfinder FRB search. The  $y$ -axis shows the Poissonian probability of seeing zero events assuming some  $\alpha$  and an expected value based on the Pathfinder rate in (Connor et al., 2016), with 45 days of observing. The rate, and therefore the expected number of detected bursts, is highly uncertain, which is why the blue region is so wide. The salmon curve shows the probability if we assume the central value of  $\mu$  predicted by Connor et al. (2016), and the dashed lines represent the  $2\sigma$  bounds. The grey shaded region at the bottom of the figure shows the region that is ruled out with 95% confidence. Assuming the salmon curve, then  $\alpha < 0.61$  is ruled out.

### False positives

Most transient searches are plagued by non-celestial sources masquerading as astronomical events. In the case of DM searches on radio telescopes, these can be caused by

RFI, numerical relics in the signal chain, or statistical fluctuations. At UTMOST, Caleb et al. (2016) found  $10^2$  events per hour in transit mode across all beams. Petroff et al. (2015) found the source of an elusive but persistent set of triggers to be due to an on-site microwave oven’s magnetron shutdown phase. These “Perytons” are unique in their conspiratorial ability to look like a real burst, but they are a subset of a broader zoo of RFI-induced false triggers.

At DRAO, although the region is officially protected from radio contamination, about 15% of the CHIME band is presently lost to RFI (see the bottom left panel of Fig. 1.9). Recently, Rogers Communications paid several billion Canadian dollars for a 700 MHz Long-Term Evolution (LTE) band for cellphone service. Unlike the satellite television stations that we see at 500-600 MHz, the LTE band fluctuates on timescales of milliseconds to seconds, which can affect a millisecond transient search. Fig. 1.9 shows an example of this RFI false positive from the LTE band.

To mitigate this, frequency channels that are known to be contaminated are masked out. Zeroing the LTE band, for instance, removed  $\sim 90\%$  of the false-positive triggers. Once this was done, we find a false-trigger rate of approximately one per two hours. This is estimated by inspecting each trigger visually. Though the rate had been greatly reduced, it is still a 1000:1 ratio of false positives to real events in the case where we detect one FRB every three months (for a detailed estimate see Sect. ?? in Chapter ??). With this in mind, the SNR threshold was increased from  $8\sigma$  to  $9\sigma$ . This was done because the false triggers tend to occur with significance very close to the cutoff. Even if they are not perfectly Gaussian, the number of  $6\sigma$  events is far larger than the number of  $8\sigma$  events, of which there are many more than  $10\sigma$  events.

This is less true for FRBs, whose brightness distribution are described by a power-law. Using a signal-to-noise cutoff of  $s_{\min}$ , the fraction of detected events one expects above  $s$  is given by,

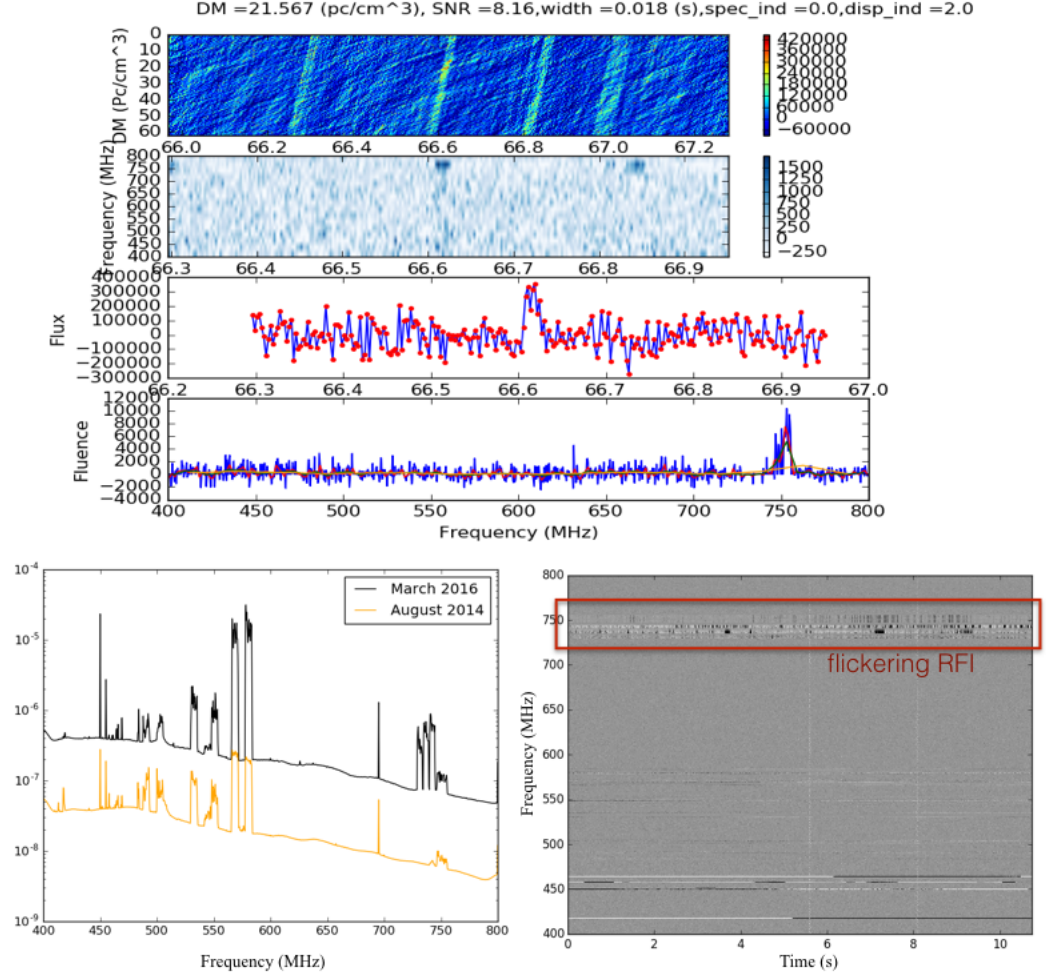


Figure 1.9: A false positive trigger caused by the flickering LTE band that, the likes of which caused  $\sim 90\%$  of the alerts before it was removed. It is of course simple to reject; one can just mask out the relevant channels. However, it provides a useful example of the types of short-timescale RFI that can affect an FRB survey.

$$f(> s) = \left( \frac{s}{s_{\min}} \right)^{-\alpha}. \quad (1.27)$$

The signal-to-noise at which  $f = 0.5$  is 12.7 and 19 for  $\alpha = 1.5$  and  $\alpha = 0.8$  respectively. The fraction of events one expects between  $8-9\sigma$  is  $f(> 8) - f(> 9) \approx 16\%$  for the Euclidean case, and  $8\%$  if  $\alpha$  is 0.8. Therefore half the true events the experiment detects will unmistakably be celestial, whether they are cosmological or Euclidean, and by increasing

the threshold to  $9\sigma$  one only decreases the survey speed by of order ten percent.

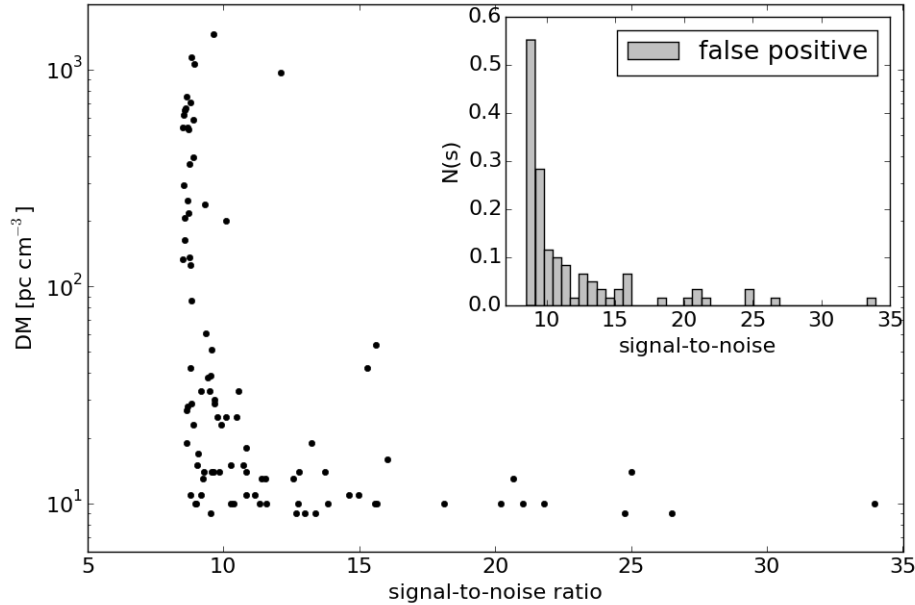


Figure 1.10: This figure shows the distribution of false-positives in DM and signal-to-noise. The embedded normalized histogram shows the clustering of events near the threshold of  $8\sigma$ . One can see that by increasing the threshold to  $\sim 9$ - $10$ , half of all false triggers could be avoided. The scatter plot shows DM vs. signal-to-noise for the same set of triggers. The high-significance tail in the histogram seem to all be clustered at very low DMs, near the minimum DM that is searched ( $10 \text{ pc cm}^{-3}$ ). This makes it easy to differentiate truly “bright” events from high-signal-to-noise false positives.

## 1.6 Conclusion

Digital beamforming is a powerful tool that affords modern radio telescopes enormous fields-of-view without sacrificing resolution. It is no longer strictly necessary to build large steerable reflectors, the cost of which scales roughly as diameter cubed<sup>5</sup>, since spatial filtering can be done in software. In this chapter we have walked through the basic mathematical formalism for beamforming. We have calculated the requisite geometric

<sup>5</sup>[https://www.astron.nl/mag/dokuwiki/lib/exe/fetch.php?media=radio\\_astronomy\\_lec.2\\_ma\\_garrett.pdf](https://www.astron.nl/mag/dokuwiki/lib/exe/fetch.php?media=radio_astronomy_lec.2_ma_garrett.pdf)

delays, which also allow us to “fringestop” the data. This process was put to use for phase-calibration of transiting point-sources, a step which is vital to beamforming.

The CHIME Pathfinder now has a stable beamforming back-end that runs in parallel with the full- $N^2$  cosmology acquisition. The back-end provides us with a tracking synthetic beam that dumps baseband data to disk with 1024 391 kHz channels at 2.56 microseconds. We have outlined the commissioning of this back-end, including the first coherent pulsar observations on CHIME.

We have also described a new project to localize FRBs with milli-arcsecond resolution using VLBI between Penticton, BC and Algonquin Park, Ontario. The first component of this project is a real-time transient search on the Pathfinder’s formed beam, which has been on-sky searching since early May 2016. Though we have not found any FRBs yet, the non-detection allows us to test the cosmological-origin hypothesis. This is because FRBs coming from  $z \approx 0.3 - 1$  will have a flatter flux distribution than a more local population, which will obey  $N(> S) \propto S^{-1.5}$ . The cosmological hypothesis implies that there exists surplus of ultra-bright bursts that could be seen by a relatively insensitive instrument like that Pathfinder. We found that with 45 days on-sky and using conservative estimates for the telescope’s sensitivity, we can rule out  $\alpha < 0.61$  with 95% confidence.

The ARO FRB search, which will complete the  $3 \times 10^3$  km baseline, was described. It has a similar set-up to the system at DRAO, except with reduced computational complexity: each packet contains all 1024 contiguous packets. Once ARO is running its search, the S/N threshold there and on the CHIME Pathfinder search will be decreased to allow for coincident detection. If both locations trigger with the same DM at the same time, baseband voltage data will be written to disk and the telescopes will be correlated against each other. This could allow for several sub-milli-arcsecond FRB detections per year.

# Bibliography

- Broten, N. W., Locke, J. L., Legg, T. H., McLeish, C. W., & Richards, R. S. 1967, Nature, 215, 38
- Caleb, M., Flynn, C., Bailes, M., et al. 2016, MNRAS, 458, 718
- Connor, L., Lin, H.-H., Masui, K., et al. 2016, MNRAS, 460, 1054
- Klages, P., Bandura, K., Denman, N., et al. 2015, ArXiv e-prints, arXiv:1503.06203
- Lorimer, D. R., Bailes, M., McLaughlin, M. A., Narkevic, D. J., & Crawford, F. 2007, Science, 318, 777
- Macovski, A. 1983, Medical Imaging Systems, Prentice-Hall information and system sciences series (Prentice-Hall)
- Petroff, E., Keane, E. F., Barr, E. D., et al. 2015, MNRAS, 451, 3933
- Thompson, A. R., Moran, J. M., & Swenson, G. W. 1986, Interferometry and synthesis in radio astronomy
- Tingay, S. J., Goeke, R., Bowman, J. D., et al. 2013, PASA, 30, e007
- van Veen, B. D., & Buckley, K. M. 1988, IEEE ASSP Magazine, 5, 4
- Vedantham, H. K., Ravi, V., Hallinan, G., & Shannon, R. 2016, ArXiv e-prints, arXiv:1606.06795



Zrnic, D. S., Kimpel, J. F., Forsyth, D. E., et al. 2007, Bulletin of the American Meteorological Society, 88, 1753